Rare Metal Materials and Engineering
Volume 55, Issue 4, April 2026
Available online at www.rmme.ac.cn

Science Press

Cite this article as: Feng Li, Zhang Xian, Ma Kai, et al. Corrosion Behavior of $FeCr_xMnAlCu$ High-Entropy Alloys in 3.5wt% NaCl Solution[J]. Rare Metal Materials and Engineering, 2026, 55(04): 877-889. DOI: https://doi.org/10.12442/j.issn.1002-185X.20250060.

ARTICLE

Corrosion Behavior of $FeCr_xMnAlCu$ High-Entropy Alloys in 3.5wt% NaCl Solution

Feng Li[1,2], Zhang Xian[1,2], Ma Kai[1,2], Zhao Yanchun[1,2], Ling Yajun[1,2], Liu Ruilong[1,2], Fu Xuan[1,2]

[1] School of Material Science and Engineering, Lanzhou University of Technology, Lanzhou 730050, China; [2] State Key Laboratory of Advanced Processing and Recycling of Nonferrous Metals, Lanzhou University of Technology, Lanzhou 730050, China

Abstract: In this study, $FeCr_xMnAlCu$ (x=0, 0.5, 1.0, 1.5, 2.0) high-entropy alloys were fabricated using vacuum arc melting, and the corrosion behavior of these alloys in 3.5wt% NaCl solution at room temperature was investigated by electrochemical dynamic potential polarization curves and immersion experiments. The microstructure results show that the high-entropy alloy with x=0 has a body-centered cubic phase structure, whereas the high-entropy alloys with x=0.5 – 2.0 have a mixed face-centered cubic+body-centered cubic dual-phase structure. The corrosion results show that the corrosion resistance of the high-entropy alloy is increased with the increase in Cr content. Among them, the high-entropy alloy with x=2.0 exhibits the optimal corrosion resistance: the highest self-corrosion potential (E_{corr}=−0.354 V vs. Ag/AgCl), the smallest self-corrosion current density (I_{corr}=1.991×10^{-6} A·cm^{-2}), and the smallest corrosion rate (0.0292 mm/a). The composite passivation film of oxides and hydroxides is formed on the surface of the corroded high-entropy alloys, and the Cr_2O_3 content is increased with the increase in Cr content, which effectively improves the stability and protective properties of the passivation film.

Key words: corrosion resistance; high-entropy alloy; passivation film; salt solution corrosion

1 Introduction

With the rapid development of science and technology, metal materials are increasingly used in aerospace, petrochemical industry, and marine environment[1–2]. The requirements for material properties become more and more stringent, especially for high hardness, high strength, good wear-resistant properties[3–4], high-temperature oxidation resistance, and corrosion resistance[5–6]. As a result, the study of high-entropy alloys (HEAs) with excellent corrosion protection has attracted considerable attention[7–8].

Generally, adding the element Cr can improve the corrosion resistance of HEAs. Yan et al[9] used vacuum arc melting to produce $Al_{0.3}Cr_xFeCoNi$ (x=0, 0.5, 1.0, 1.5, 2.0) alloys. In the 3.5wt% NaCl solution, the effects of different Cr concentrations on the microstructure and corrosion behavior of the HEAs were investigated. The result showed that increasing Cr concentration decreased the corrosion rate and self-corrosion current density I_{corr}, whereas the self-corrosion potential E_{corr}, pitting resistance, and charge transfer resistance were increased. Notably, a protective oxide film of Cr_2O_3 formed on the surface of $Al_{0.3}Cr_2FeCoNi$ HEAs which were characterized by a Cr-rich phase. The protective oxide film exhibited high corrosion resistance. Ge et al[10] studied the effect of different Cr contents on the microstructure and corrosion resistance of $(FeCoNi)_{75-x}Cr_xB_{15}Si_{10}$ HEA coatings and found that the corrosion resistance is constantly increased when the Cr concentration increased. The enhanced corrosion resistance can be attributed to the improvement of the boride composition and the formation of the interdendrite (ID) region caused by Cr addition into HEAs, thus mitigating localized corrosion phenomenon. Chai et al[11] studied the cast structure

Received date: April 08, 2025
Foundation item: Gansu Provincial Science and Technology Major Special Program (24ZDWA008); Fourth Batch of Top Leading Talents Fund Projects in Gansu Province (ZZ2023G50100013)
Corresponding author: Feng Li, Ph. D., Professor, School of Materials Science and Engineering, Lanzhou University of Technology, Lanzhou 730050, P. R. China, E-mail: fenglils@lut.edu.cn

and corrosion behavior of $FeCoNiCr_x$ alloy with different Cr contents and found that $FeCoNiCr_{0.5}$ alloy exhibits remarkable resistance against corrosion in 3.5wt% NaCl solution, whereas excess Cr caused significant localized corrosion in $FeCoNiCr_{0.5}$ alloy. Ren et al[12] studied the effect of different Cr concentrations on the corrosion behavior of the $CoCr_xCuFeMnNi$ HEAs. The results showed that both the I_{corr} and average corrosion rate of the alloy are reduced, and its corrosion resistance is improved when the Cr concentration increased. This improvement in corrosion resistance is attributed to the stable dense Cr_2O_3 passivation film on the material surface. It is also reported that the element Cr is a crucial component in the development of HEA composition and it is indispensable to the excellent corrosion resistance of HEAs.

The corrosion resistance of FeCrMnAlCu series HEAs is widely researched[7,13–14]. It is revealed that the variation in addition elements for HEAs significantly influences the corrosion resistance of FeCrMnAlCu HEAs. However, the effect of varying Cr content on the corrosion resistance of the FeCrMnAlCu HEAs in the 3.5wt% NaCl solution remains unclear. Therefore, in this research, five elements—Fe, Cr, Mn, Al, and Cu—were used as raw materials for the synthesis of $FeCr_xMnAlCu$ HEAs. $FeCr_xMnAlCu$ (x=0, 0.5, 1.0, 1.5, 2.0) HEAs were fabricated using vacuum arc melting technique. To optimize the composition and corrosion resistance of $FeCr_xMnAlCu$ HEAs, the impact of Cr content on corrosion resistance was analyzed. Additionally, the corrosion behavior of the alloy in 3.5wt% NaCl solution was investigated.

2 Experiment

2.1 Preparation of $FeCr_xMnAlCu$ HEAs

In this study, metal particles of Fe, Cr, Mn, Al, and Cu (purity exceeding 99.9%) were used as melting raw materials. The element contents in $FeCr_xMnAlCu$ HEAs are listed in Table 1. The $FeCr_xMnAlCu$ HEAs with x=0, 0.5, 1.0, 1.5, and 2.0 were denoted as Cr_0, $Cr_{0.5}$, $Cr_{1.0}$, $Cr_{1.5}$, and $Cr_{2.0}$, respectively. The HEA was produced using non-self-consuming vacuum arc melting technique. The oxide layer on the surface of the metal particles was removed by polishing to prevent contaminants before melting. High-purity argon served as the protective atmosphere during the melt process, and the vacuum was controlled as 2.5×10^{-3} Pa. To achieve chemical homogeneity of the ingot, the molten alloy was repeatedly melted 4–5 times.

Table 1 Element content in $FeCr_xMnAlCu$ HEAs (wt%)

Alloy	Fe	Cr	Mn	Al	Cu
Cr_0	27.73	-	27.29	13.41	31.57
$Cr_{0.5}$	24.57	11.44	24.17	11.87	27.95
$Cr_{1.0}$	22.05	20.53	21.68	10.65	25.09
$Cr_{1.5}$	19.99	27.92	19.67	9.67	22.75
$Cr_{2.0}$	18.29	34.06	18.00	8.84	20.81

To precisely predict the microstructure and phase formation of $FeCr_xMnAlCu$ HEAs, important parameters, such as mixing entropy (ΔS_{mix}), enthalpy of mixing (ΔH_{mix}), atomic size difference (δ), and valence electron concentration (VEC), should be considered[15–17]. The calculation formulas of ΔS_{mix}, ΔH_{mix}, δ, and VEC are expressed by Eq.(1–4), respectively. Among these parameters, the mixing entropy is closely correlated with the propensity of the alloy to form solid solution phases. The alloy is classified as HEAs[18] when $\Delta S_{mix}>1.5R$ with R as the gas constant. The ΔH_{mix} is used to determine the compatibility of the alloying components, whereas the atomic size difference influences the stability of the solid solution and the potential for phase separation. HEAs are prone to the formation of stable solid solution structures under the conditions of $-15\ kJ\cdot mol^{-1}\leqslant\Delta H_{mix}<5\ kJ\cdot mol^{-1}$ and $\delta\leqslant6.6\%$[16,19]. In addition, VEC is correlated with the electronic structure and overall properties of the alloys. When VEC is below 6.87, the body-centered cubic (bcc) phase is more likely to form[16]. These parameters influence the formation of the solid solution structure of HEAs. Table 2 displays the essential parameter calculation results for $FeCr_xMnAlCu$ HEAs.

$$\Delta S_{mix} = -R\sum_{i}^{n} c_i \ln c_i \tag{1}$$

$$\Delta H_{mix} = \sum_{i=1,i\neq j}^{n} \Omega_{ij}^{mix} c_i c_j \text{ with } \Omega_{ij}^{mix} = 4H_{ij}^{mix} \tag{2}$$

$$\delta = 100\sqrt{\sum_{i=1}^{n} c_i\left(1-\frac{r_i}{\bar{r}}\right)^2} \text{ with } \bar{r} = \sum_{i=1}^{n} c_i r_i \tag{3}$$

$$\mathrm{VEC} = \sum_{i=1}^{n} c_i\,(\mathrm{VEC})_i \tag{4}$$

where H_{ij}^{mix} is the binary mixing enthalpy between different elements, n is the number of elements, c_i is the percentage of ith element in the alloy, R is the gas constant (8.314 $J\cdot mol^{-1}\cdot K^{-1}$), r_i is the difference in atomic radius of the ith element, and $(VEC)_i$ is the number of valence electrons of the ith element.

2.2 Microstructure characterization

The crystal structures of specimens were analyzed using an X-ray diffractometer (XRD, D/max-2400, Cu target, Kα λ = 0.154 nm). The scanning parameters were as follows: the scanning angle (2θ) ranged from 20° to 90° with a scanning speed of 4°/min, and the scanning step size was 0.02°. The morphology and microstructure of specimens were observed using scanning electron microscope (SEM, Quanta FEG450) and transmission electron microscope (TEM, Talos F200X),

Table 2 Parameter values of standard conditions for $FeCr_xMnAlCu$ HEAs

Alloy	ΔH_{mix}/kJ·mol^{-1}	ΔS_{mix}/kJ·mol^{-1}	δ/%	VEC
Cr_0	−7.000	11.523	4.816	7.250
$Cr_{0.5}$	−4.840	13.144	4.727	7.111
$Cr_{1.0}$	−3.520	13.377	4.624	7.000
$Cr_{1.5}$	−6.998	13.253	4.515	6.909
$Cr_{2.0}$	−10.850	12.978	4.407	6.833

respectively. The element distribution on the surface was detected using energy-dispersive spectroscope (EDS). The chemical valence states of the surface elements (Al, Cr, Fe, Mn, Cu, and O) were analyzed using X-ray photoelectron spectroscope (XPS, Thermo ScientificTM K-AlphaTM+, Al-Kα, 1486.6 eV). The experiment data were fitted and analyzed using Avantage software, and the spectral peaks were calibrated using the binding energy of C 1s (284.8 eV). Each element was fitted to the National Institute of Standards and Technology (NIST) XPS database.

2.3 Electrochemical tests

A CHI 760E electrochemical workstation with a conventional three-electrode system was used for the tests. The HEAs with varying Cr content served as the working electrode, a thin Pt sheet was used as the counter electrode, and Ag/AgCl was used as the reference electrode. Copper wires were soldered to alloy specimens (10 mm×10 mm×3 mm) with tin wire and covered with epoxy resin, and only the working surface (10 mm×10 mm) was exposed. Then, the specimen surface was sanded with different types of sandpaper, then polished, cleaned, and dried. The specimens were submerged in a 3.5wt% NaCl solution for 3600 s. Until reaching a steady state, the open circuit potential was determined at the sampling interval of 0.1 s.

Electrochemical impedance spectroscopy (EIS) experiments under open circuit potential were conducted at an amplitude of 5 mV and a frequency range of 10^5 – 0.001 Hz on alloy specimens at room temperature. Z-View software was then used to fit these EIS data and assess the electrochemical corrosion properties of specimens.

Potentiodynamic polarization (PDP) test was performed on the specimens at the potential scan ranging from − 1.5 V vs. Ag/AgCl to 1.0 V vs. Ag/AgCl, scan rate of 0.01 V/s, and room temperature. To confirm the reliability of the electrochemical test results, three parallel specimens were used in each set to ensure data accuracy.

2.4 Soaking experiment

Before the immersion test, the volume of the specimen was measured using the drainage method, and the density of the alloy was calculated according to Archimedes' principle, which is the foundation for the subsequent calculation of the corrosion rate. The corrosion rate was determined by immersing the specimens into the 3.5wt% NaCl solution for 168 h. During the immersion, the solution was changed every 24 h to ensure its validity and stability. After the solution was changed each time, the surface of each specimen was cleaned with deionized water. Subsequently, the specimens were dried, and their mass was measured using an electronic scale with the precision of 0.0001 g to determine the mass loss before and after corrosion. According to the American Society for Testing Materials standard G31-72, the volume ratio of NaCl solution used in the experiment to the surface area of the specimen was strictly controlled as above 0.20 mL/mm^2 to ensure the validity of the experiment conditions[20].

3 Results and Discussion

3.1 Microstructure analysis

Fig. 1a shows XRD patterns of the FeCr$_x$MnAlCu HEAs. It can be noticed that the Cr$_0$ alloy exhibits a single bcc phase structure. However, the addition of the element Cr alters the phase structure of other alloys. In addition to the original bcc phase, face-centered cubic (fcc) phase is also formed, and a new Laves phase starts to precipitate. Through quantitative analysis of the changes in diffraction peak intensity, it was found that when the Cr content $x \leqslant 1$, the diffraction peak intensities of bcc and fcc phases are increased with the increase in Cr content; when $x>1$, the diffraction peak intensities of both bcc and fcc phases are decreased with the increase in Cr content. This phenomenon indicates that the addition of Cr has a significant regulatory effect on the phase structure of the alloy, i. e., the Cr content promotes the formation of the bcc phase[21]. According to Fig. 1b, it can be found that the characteristic peak (110) of bcc phase shifts to the right side with the addition of Cr. This phenomenon is mainly attributed to the difference in atomic radius between Cr and other elements, which leads to severe lattice distortion[22].

Fig. 2 depicts SEM images of different FeCr$_x$MnAlCu HEAs. A typical equiaxial crystal structure can be observed in Cr$_0$ specimen. However, Cr$_{0.5}$, Cr$_{1.0}$, Cr$_{1.5}$, and Cr$_{2.0}$ specimens have dendrite (DR) and ID structures. As Cr content increases, the primary DR arms in the alloys gradually become thinner and shorter, whereas the secondary DR arms eventually disappear.

Fig. 3 depicts SEM images and corresponding EDS element distributions of FeCr$_x$MnAlCu HEAs with x=0, 0.5, and 2.0.

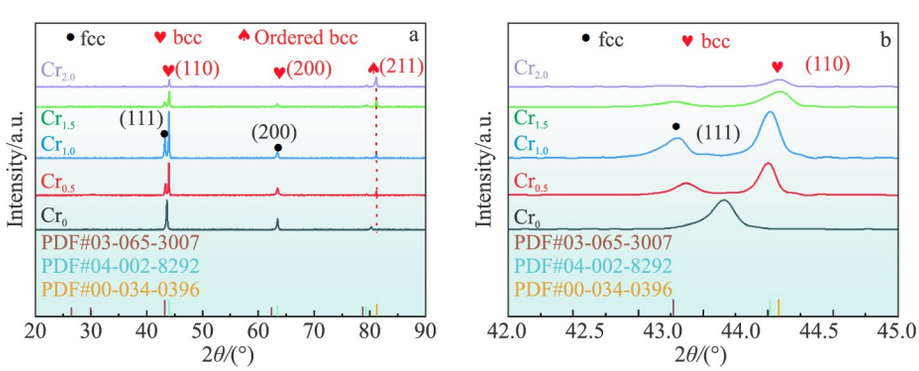

Fig.1 XRD patterns of different FeCr$_x$MnAlCu HEAs: (a) 2θ=20°–90°; (b) 2θ=42.0°–45.0°

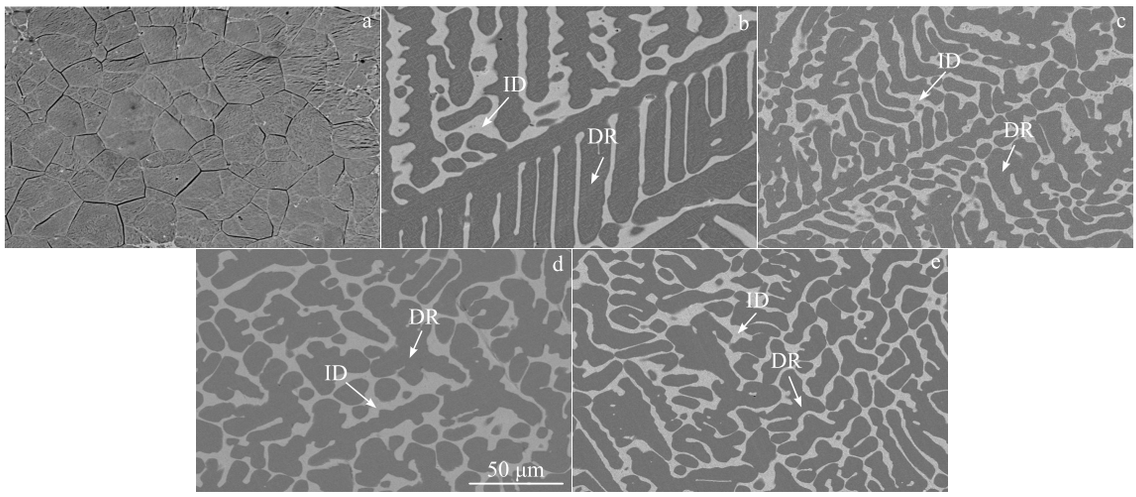

Fig.2 SEM morphologies of different $FeCr_xMnAlCu$ HEAs: (a) Cr_0, (b) $Cr_{0.5}$, (c) $Cr_{1.0}$, (d) $Cr_{1.5}$, and (e) $Cr_{2.0}$

In the Cr_0 specimen, the element Al is uniformly distributed and no discernible segregation phenomenon occurs. Elements Fe and Mn are dispersed in the center region of the equiaxial crystals, and the element Cu is segregated around the grain boundaries of equiaxial crystals. In the $Cr_{0.5}$ and $Cr_{2.0}$ specimens, elements Fe, Cr, and Mn are mainly distributed in DRs, the element Cu is mainly distributed between DRs, whereas the element Al is evenly distributed without significant segregation.

To reveal the chemical composition of the precipitated phases and matrix in the alloy, the $Cr_{2.0}$ specimen is analyzed using TEM coupled with selected area electron diffraction (SAED) analyses. As shown in Fig. 4a – 4f, the matrix in the DR region is a disordered FeCr solid solution. In addition, uniform long streaks of precipitates are distributed in DR region, which are identified as ordered $Al_{0.25}Cu_{0.75}$ intermetallic compounds, whereas the ID structure is identified as disordered $AlCu_2Mn$. Fig. 4c and 4f reveal DR (200) and ID (220) interfacial spacings, which are determined by the fast Fourier transform (FFT) patterns and inverse Fourier transform (IFT) patterns, respectively. The DR (200) and ID (220) interfacial spacings are measured as 0.149 and 0.210 nm, respectively. As shown in Fig. 4h – 4l, Fe, Cr, and Mn are concentrated in the region of DR crystals, whereas Cu is mainly dispersed in ID region. However, the element Al shows no clear segregation and is uniformly distributed. This observation is consistent with the SEM and EDS analysis results. Fig. 4m shows the element contents, and Fig. 4n – 4r show EDS element distributions of the precipitated phase, further confirming that the precipitated phase has AlCu bcc structure.

The crystallographic properties of $FeCr_xMnAlCu$ HEAs are analyzed using electron back-scattered diffraction (EBSD) technique. As shown in Fig. 5, the inverse phase figures (IPFs) of the five alloys all show randomly distributed crystal orientations, and the grain size shows a clear refinement trend with increasing Cr content[23], which may be attributed to the effect of solutes on grain growth during solidification. Quantitative analysis shows that the average grain sizes of the Cr_0, $Cr_{0.5}$, $Cr_{1.0}$, $Cr_{1.5}$, and $Cr_{2.0}$ specimens are 117.4, 102.1, 96.3, 90.4, and 84.3 μm, respectively. TEM analysis also shows that the $Cr_{2.0}$ specimen contains an $Al_{0.25}Cu_{0.75}$ precipitated phase. These nanoscale precipitation phases have a pinning effect on the grain boundaries, thereby effectively inhibiting grain growth. These properties indicate that the grain structure of the alloy is refined with the increase in Cr content.

3.2 Electrochemical corrosion behavior

The PDP curves, EIS curves, and fitted equivalent circuit diagrams of $FeCr_xMnAlCu$ HEAs in 3.5wt% NaCl solution are displayed in Fig. 6. As shown in Fig. 6a, five specimens all exhibit strong passivation phenomena: Cr_0 specimen exhibits wider passivation regions, while $Cr_{0.5}$, $Cr_{1.0}$, $Cr_{1.5}$, and $Cr_{2.0}$ specimens exhibit narrower passivation regions. It is also found that all five specimens exhibit an activation-passivation-transition passivation zone without an obvious active dissolution zone, which demonstrates spontaneous passivation in aqueous solution for the five specimens. PDP curve was analyzed using the Tafel method[24], and the resulting electrochemical corrosion parameters are shown in Table 3. The results show that the E_{corr} and polarization resistance (R_p) are steadily increased, whereas I_{corr} is steadily reduced with the increase in Cr content. It is shown that the element Cr is favorable to the corrosion resistance of the alloy. Among these HEAs, $Cr_{2.0}$ specimen has the highest E_{corr} (− 0.354 V vs. Ag/AgCl), the largest R_p value (8622.6 Ω ·cm^2), and the smallest I_{corr} (1.991×10^{-6} A · cm^{-2}), indicating that it exhibits superior corrosion resistance[12].

Nyquist and Bode plots of the $FeCr_xMnAlCu$ HEAs are shown in Fig. 6b – 6d. As shown in Fig. 6b, all specimens exhibit similar semicircular arcs. The radius of the capacitance arc of different $FeCr_xMnAlCu$ HEAs is in the following order: $Cr_{2.0}>Cr_{1.5}>Cr_{1.0}>Cr_{0.5}>Cr_0$. It shows that the corrosion resistance of the alloys is improved with the addition of element Cr[25]. As shown in Fig. 6c, the phase angle of the $FeCr_xMnAlCu$ HEAs is gradually increased with the increase in Cr content, indicating that the presence of a passivation

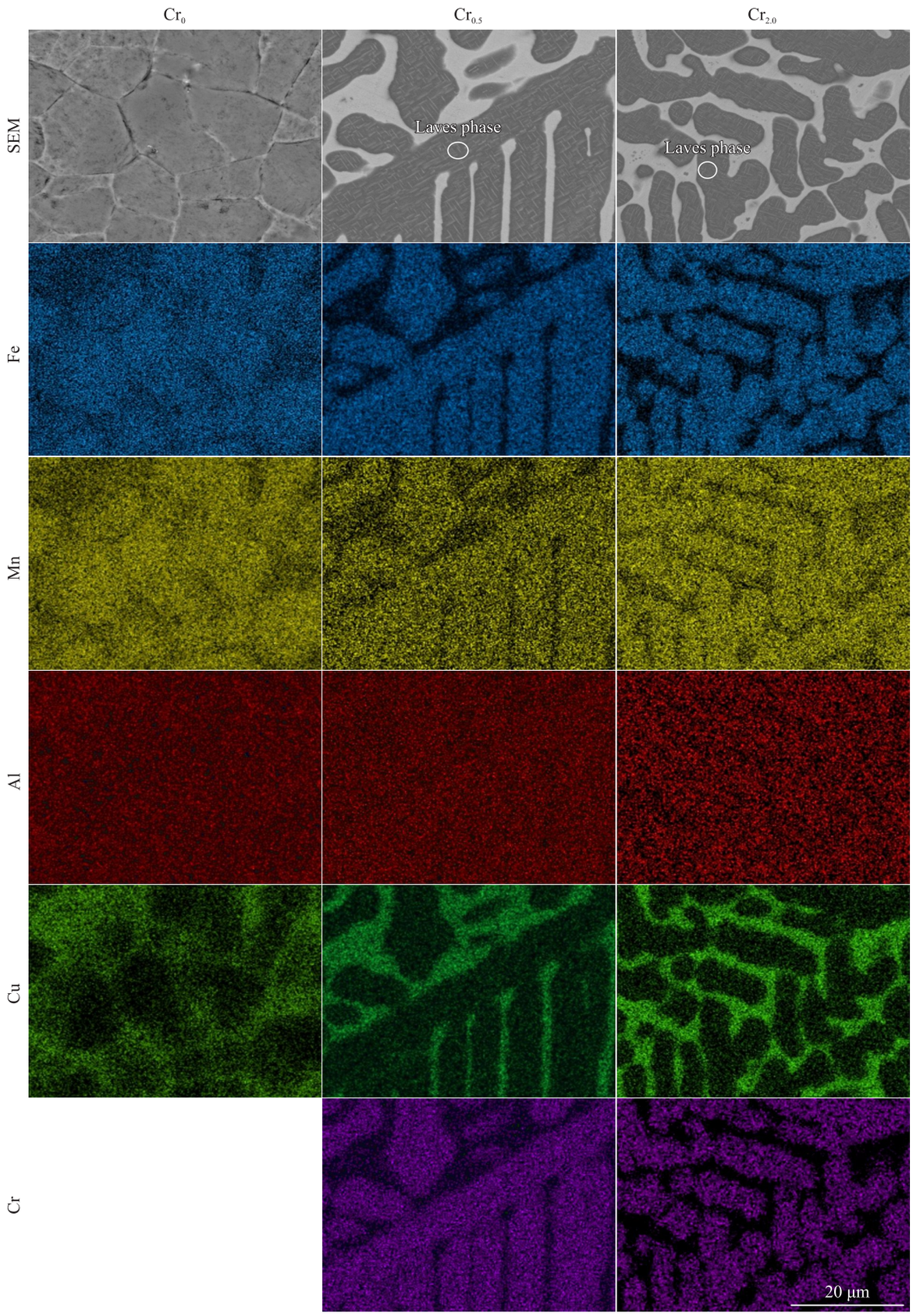

Fig.3 SEM images and corresponding EDS element distributions of different $FeCr_xMnAlCu$ HEAs

film is related to the capacitive response. In addition, it can be seen from Fig. 6d that the impedance modulus of $FeCr_xMnAlCu$ HEAs is increased with the increase in Cr content. This further confirms that the addition of element Cr is beneficial to the corrosion resistance of the $FeCr_xMnAlCu$ HEAs in 3.5wt% NaCl solution. Besides, $Cr_{2.0}$ HEA has the

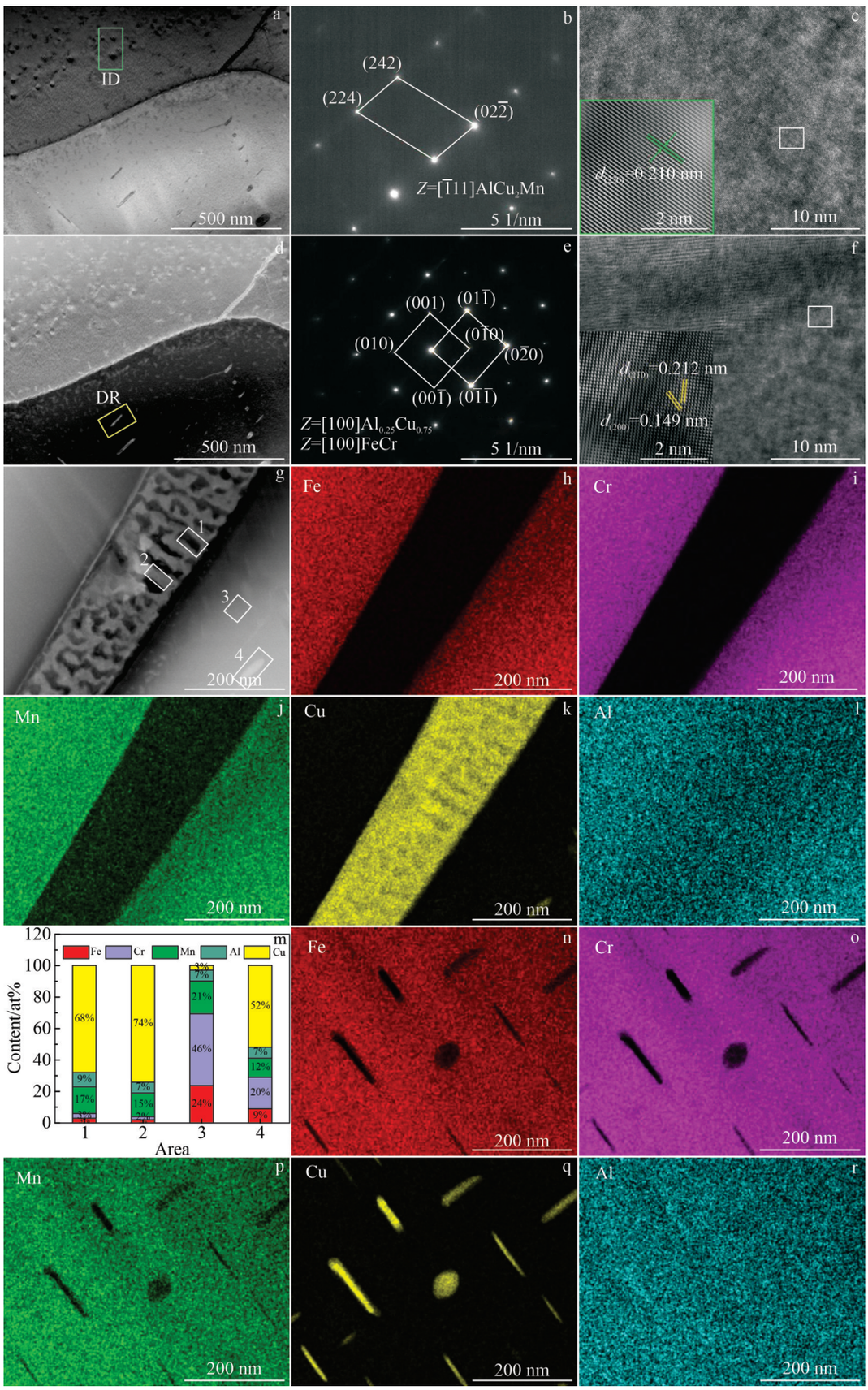

Fig.4 TEM analysis of $Cr_{2.0}$ specimen: (a) bright-field image; (b) SAED pattern corresponding to green rectangular area in Fig. 4a; (c) high resolution TEM image corresponding to green rectangular area in Fig.4a with FFT pattern; (d) dark-field TEM image; (e) SAED pattern corresponding to yellow rectangular area in Fig.4d; (f) high resolution TEM image corresponding to yellow rectangular area in Fig.4d with IFT pattern; (g) high-angle annular dark field phase image; (h–l) EDS element distributions corresponding to Fig.4g; (m) element contents of marked areas in Fig.4g; (n–r) EDS element distributions corresponding to yellow rectangular area in Fig.4d

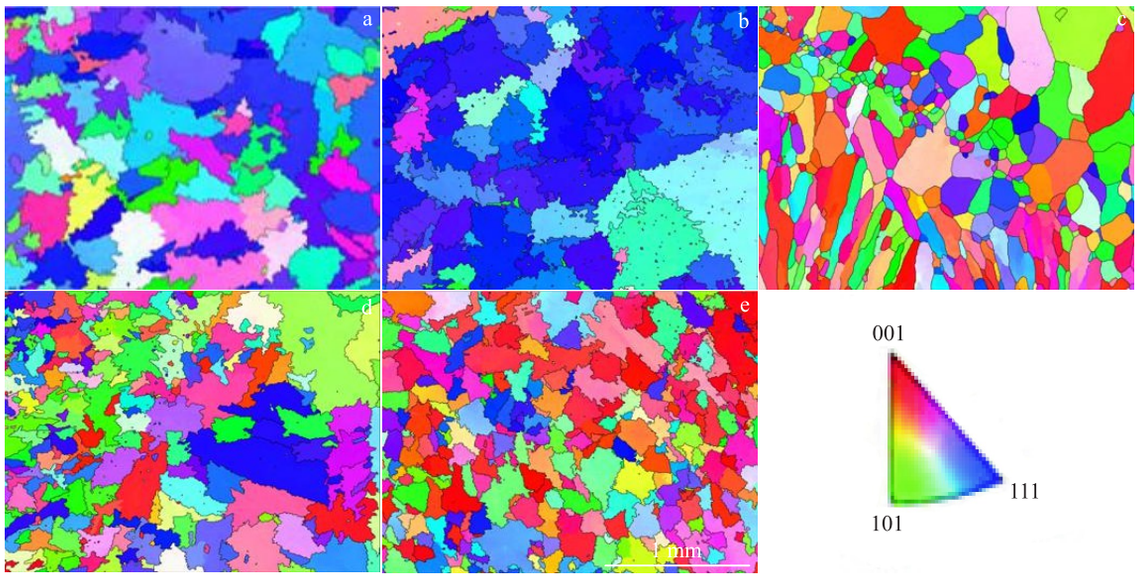

Fig.5 IPFs of different $FeCr_xMnAlCu$ HEAs: (a) Cr_0, (b) $Cr_{0.5}$, (c) $Cr_{1.0}$, (d) $Cr_{1.5}$, and (e) $Cr_{2.0}$

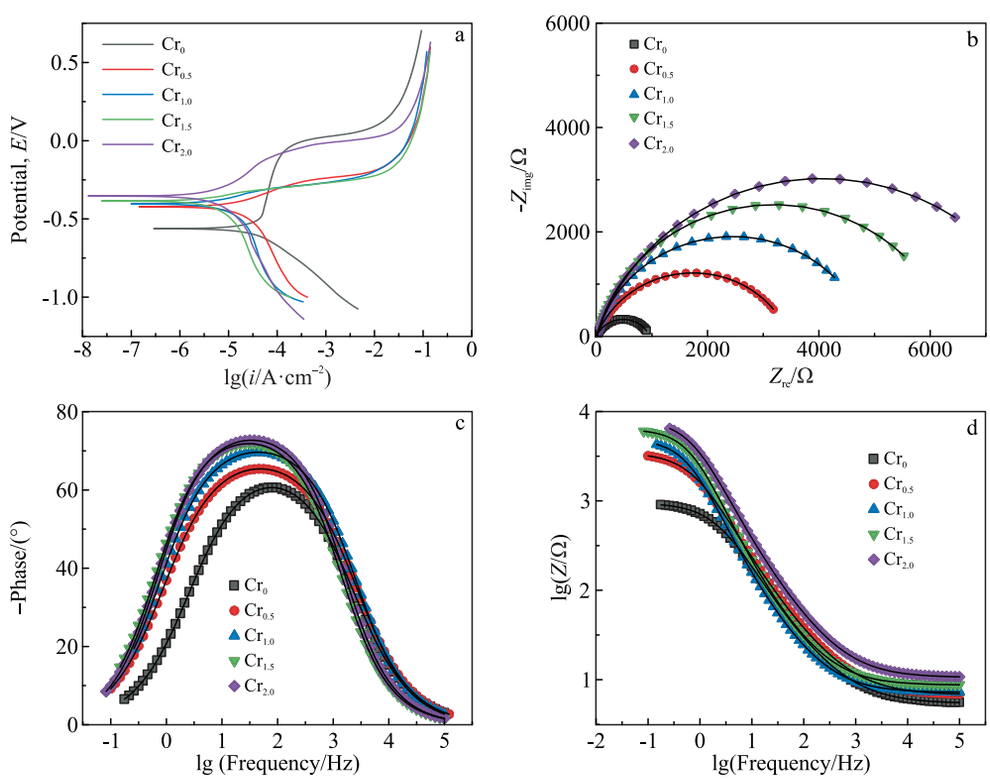

Fig.6 Electrochemical results of $FeCr_xMnAlCu$ HEAs: (a) PDP curves; (b) Nyquist plots; (c) Bode phase angles; (d) Bode plots

Table 3 Electrochemical parameters of $FeCr_xMnAlCu$ HEAs

Alloy	E_{corr}/V vs. Ag/AgCl	I_{corr}/A·cm^{-2}	R_p/Ω·cm^2
Cr_0	−0.687	5.603×10^{-5}	1108.7
$Cr_{0.5}$	−0.472	1.424×10^{-5}	2337.5
$Cr_{1.0}$	−0.413	3.423×10^{-6}	5023.2
$Cr_{1.5}$	−0.376	2.498×10^{-6}	6661.4
$Cr_{2.0}$	−0.354	1.991×10^{-6}	8622.6

optimal corrosion resistance.

Fig. 7 shows the equivalent circuit model of $FeCr_xMnAlCu$ HEAs, which is used to fit EIS results. In this case, R_s represents the electrolyte solution resistance, CPE is the constant phase-angle element, and R_{ct} is the electrode charge transfer resistance. Due to the existence of defects and other states in the alloy, the flashlight response of the alloy is not completely ideal capacitance behavior. Thus, CPE is introduced to replace the capacitance response of the alloy in solution[26–27]. The value of Z_{CPE} can be calculated using Eq.(5), as follows:

$$Z_{CPE} = Y_0^{-1}(j\omega)^{-n} \quad (5)$$

where Y_0 (Y_0>0), j, and ω denote the scale factor, imaginary

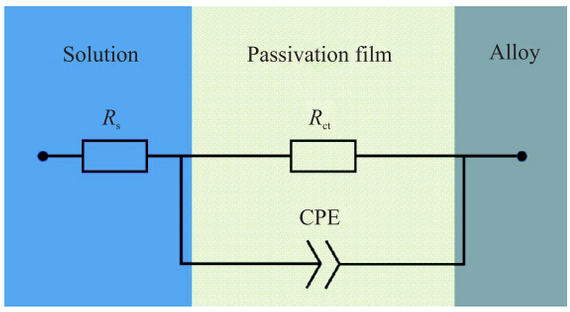

Fig.7 Equivalent circuit model of $FeCr_xMnAlCu$ HEAs

unit, and angular frequency, respectively; n is an index of surface inhomogeneity. The subscript CPE is denoted as a pure resistance when n=0, and the CPE is denoted as a pure capacitor when n=1. The Bode plot shows that the equivalent circuit fitting results are consistent with the experiment results.

As shown in Table 4, R_{ct} values of the $FeCr_xMnAlCu$ HEAs are gradually increased with the increase in Cr content due to the formation of a dense and homogeneous passivation film on the surface. The $Cr_{2.0}$ specimen exhibits the highest R_{ct} value (8084 $\Omega \cdot cm^2$), indicating that ions in the electrolyte solution are more difficult to flow through the passivation film layer, and therefore providing the optimal corrosion resistance. This result is consistent with the PDP curve results. In addition, the value of n is between 0.5 and 0.8, which indicates that the capacitance deviates from the ideal state,

Table 4 Fitting results of impedance for $FeCr_xMnAlCu$ HEAs

Alloy	R_s/Ω·cm	R_{ct}/Ω·cm	CPE/$\Omega^{-1}\cdot s^n\cdot cm^{-2}$	n
Cr_0	5.43	954	1.25×10^{-4}	0.76
$Cr_{0.5}$	6.78	3465	1.87×10^{-4}	0.78
$Cr_{1.0}$	7.22	4890	6.35×10^{-5}	0.85
$Cr_{1.5}$	8.72	6366	4.38×10^{-5}	0.86
$Cr_{2.0}$	10.62	8084	3.39×10^{-5}	0.82

which is mainly due to the inhomogeneous corrosion layer on the specimen surface[28].

Fig. 8 shows SEM surface images of $FeCr_xMnAlCu$ HEAs in 3.5wt% NaCl solution after electrochemical corrosion. The results show that the corrosion of $FeCr_xMnAlCu$ HEAs is more severe at the interface between DR and ID regions. As shown in Fig. 8a, the surface of the corroded Cr_0 specimen is rough, exhibiting severe grain boundary corrosion and numerous corrosion pits. Compared with those of the Cr_0 specimen, the corrosion degree and area of other specimens are gradually decreased with the increase in Cr content, as shown in Fig. 8b–8e. In the corroded $Cr_{0.5}$ and $Cr_{1.0}$ specimens, wider corrosion crevices appear at the interface because the addition of element Cr promotes a more homogeneous corrosion behavior, thus reducing the formation of localized corrosion craters. A slight localized corrosion can be observed on the surface of corroded $Cr_{1.5}$ and $Cr_{2.0}$ specimens. Their corrosion crevices gradually narrow. This phenomenon indicates that the $Cr_{2.0}$ HEA has superior corrosion resistance. This finding is also consistent with the results of PDP curve.

The details of the chemical characteristics before corrosion were further analyzed using XPS. Fig. 9 – Fig. 11 show XPS spectra of the surface of $FeCr_xMnAlCu$ HEAs after electrochemical corrosion in 3.5wt% NaCl solution. The spectra of Al $2p_{3/2}$, Cr $2p_{3/2}$, Fe $2p_{3/2}$, Mn $2p_{3/2}$, Cu $2p_{3/2}$, and O 1s are all revealed, and these spectra are fitted for the compounds involved according to NIST database. It can be seen that the Al $2p_{3/2}$ spectra contain the information of metallic Al^0 (72.2 eV) and Al^{3+} (74.5 eV). The passivation film formed by Al under natural conditions is expressed by Eq.(6):

$$2Al + 3H_2O \rightarrow Al_2O_3 + 6H^+ + 6e^- \quad (6)$$

The Mn $2p_{3/2}$ spectra consist of Mn^0 (639 eV), Mn^{2+} (640.5 eV), and Mn^{3+} (642 eV). Mn^{2+} is related to MnO and $Mn(OH)_2$, whereas Mn^{3+} is related to Mn_2O_3 and MnOOH. The Cr $2p_{3/2}$ spectra are separated into metallic Cr^0 (574.7 eV),

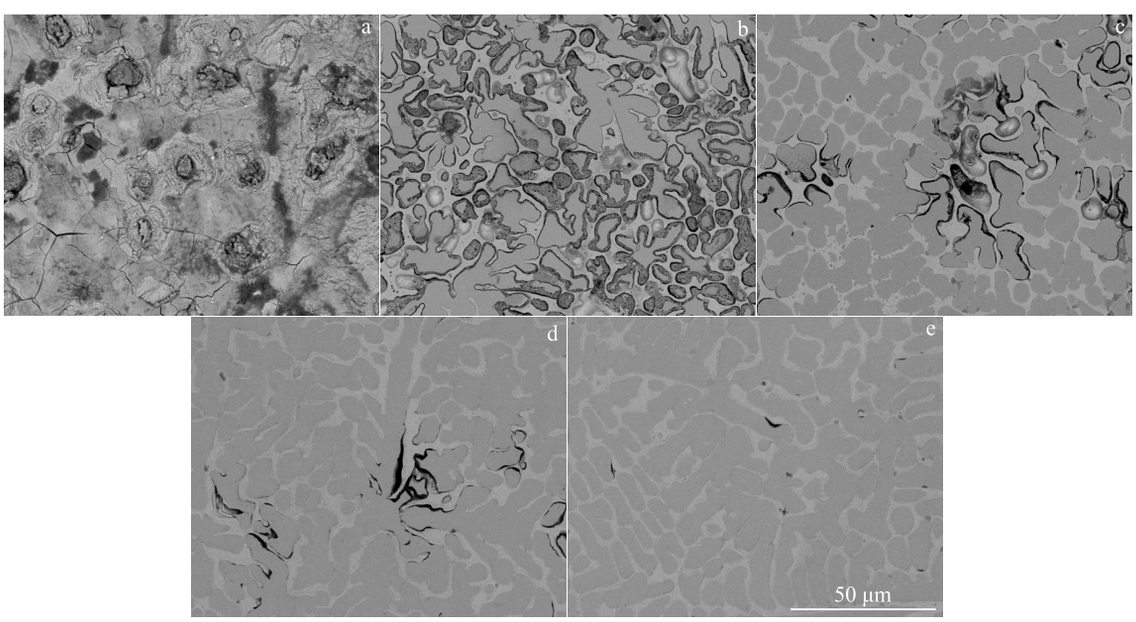

Fig.8 SEM surface images of different $FeCr_xMnAlCu$ HEAs after electrochemical experiments: (a) Cr_0, (b) $Cr_{0.5}$, (c) $Cr_{1.0}$, (d) $Cr_{1.5}$, and (e) $Cr_{2.0}$

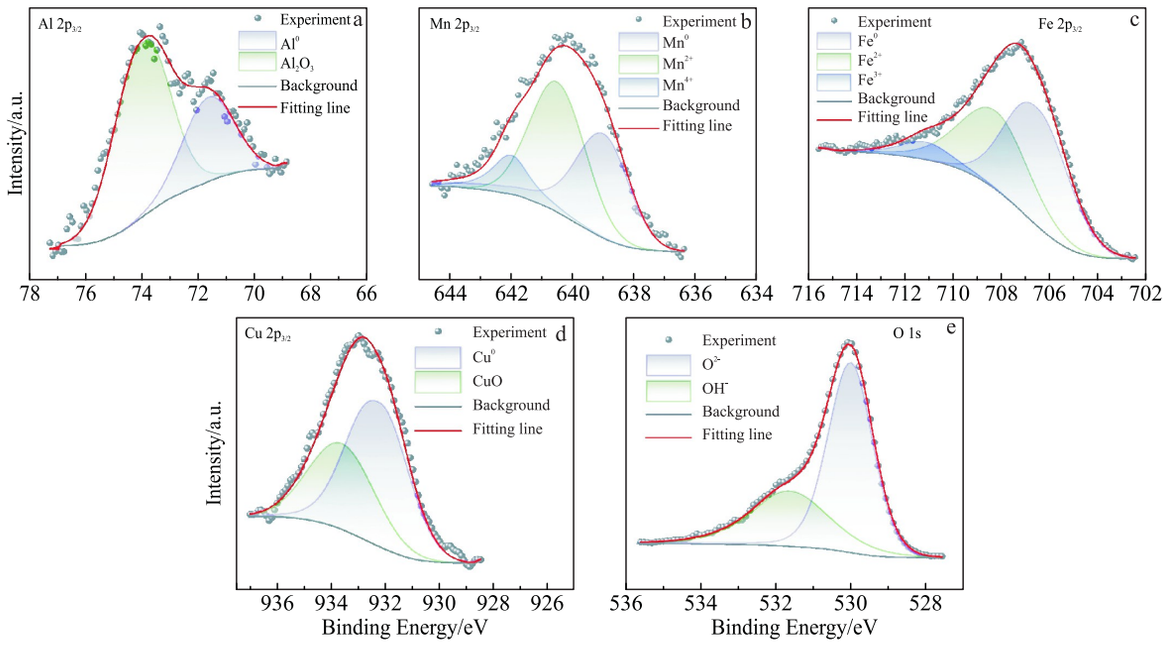

Fig.9 XPS spectra of Cr_0 specimen after corrosion: (a) Al; (b) Mn; (c) Fe; (d) Cu; (e) O

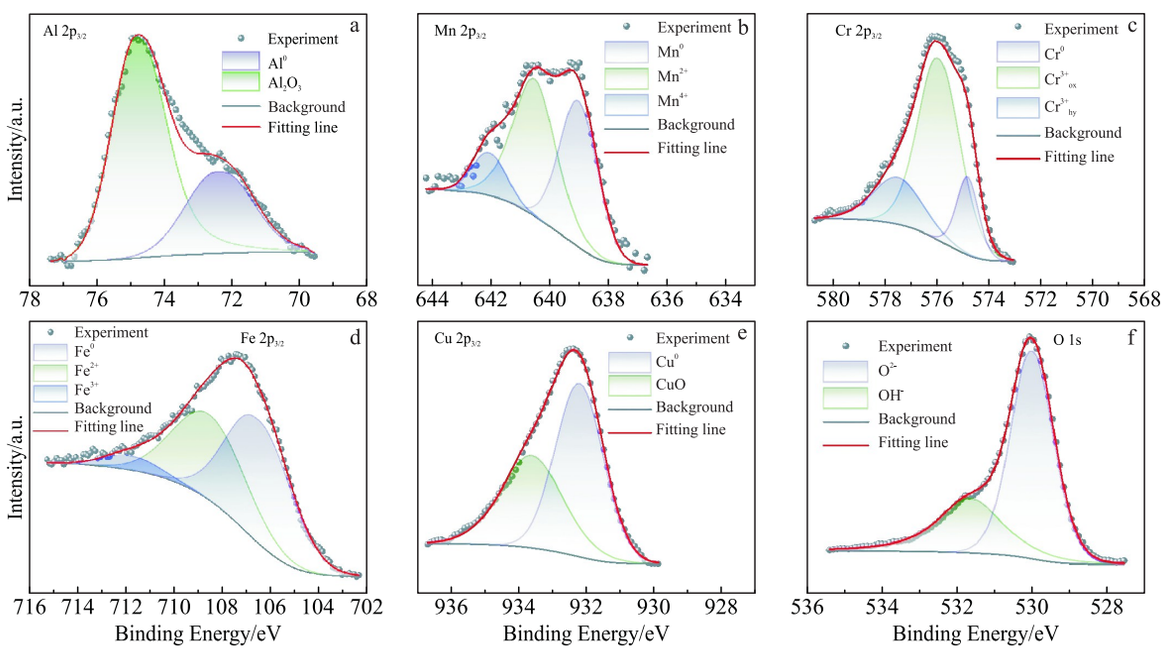

Fig.10 XPS spectra of $Cr_{0.5}$ specimen after corrosion: (a) Al; (b) Mn; (c) Cr; (d) Fe; (e) Cu; (f) O

Cr_{ox}^{3+} (575.9 eV) and Cr_{hy}^{3+} (577.4 eV) peaks. Among them, the de-hydroxylation reaction converts $Cr(OH)_3$ to Cr_2O_3[29]. A similar phenomenon can be observed in the Cr-doped HEAs[30]. Due to the high-oxygen affinity of Cr and the thermodynamic stability of Cr_2O_3, the Cr_2O_3 in the passivation film provides an effective protective barrier to the corrosion resistance of the alloy[31]. Fig. 8 shows that the addition of element Cr increases the content of Cr_2O_3 in the passivation film, which effectively protects the alloy matrix from Cl^- erosion, and the $Cr_{2.0}$ specimen shows excellent corrosion resistance. The formation of Cr_2O_3-rich passivation films is attributed to the reactions expressed in Eq.(7–8):

$$Cr^{3+} + 3H_2O \leftrightarrow Cr(OH)_3 + 3H^+ \quad (7)$$

$$Cr(OH)_3 + Cr \rightarrow Cr_2O_3 + 3H^+ + 3e^- \quad (8)$$

In addition, three peaks are identified in the Fe $2p_{3/2}$ spectra: metallic Fe^0 (706.5 eV), Fe^{2+} (708.2 eV), and Fe^{3+} (711.6 eV). In NaCl solution, Fe is preferentially dissolved as a low valence cation, immediately followed by hydrolysis and oxidation in the electrolyte solution, forming a variety of oxides and hydroxides, as expressed by Eq.(9–12):

$$Fe^{2+} + 2H_2O \leftrightarrow Fe(OH)_2 + 2H^+ \quad (9)$$

$$Fe(OH)_2 \rightarrow FeO + H_2O \quad (10)$$

$$4Fe^{2+} + O_2 + 2H_2O \rightarrow 4Fe^{3+} + 4OH^- \quad (11)$$

$$2Fe^{3+} + 6OH^- \rightarrow Fe_2O_3 + 3H_2O \quad (12)$$

The Cu $2p_{3/2}$ spectra are divided into two peaks: Cu^0 (932.2

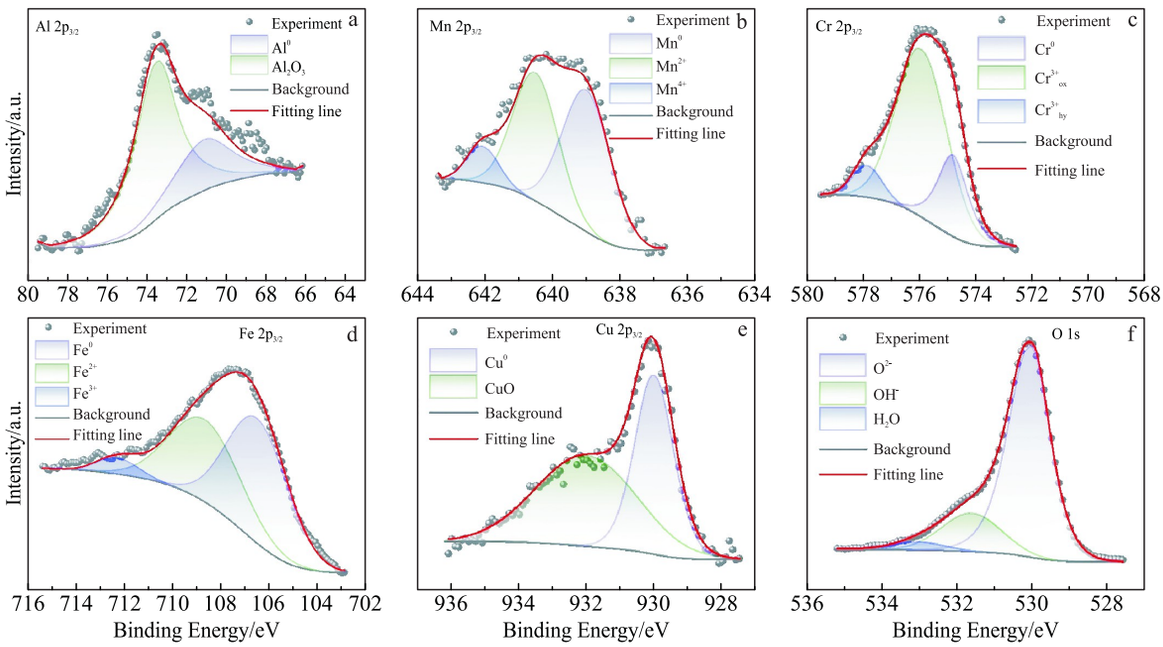

Fig.11 XPS spectra of $Cr_{2.0}$ specimen after corrosion: (a) Al; (b) Mn; (c) Cr; (d) Fe; (e) Cu; (f) O

eV) and Cu^{2+} (933.1 eV). Cu^{2+} is hydrolyzed in an electrolyte solution, as expressed by Eq.(13):

$$Cu^{2+} + H_2O \leftrightarrow CuO + 2H^+ \quad (13)$$

The predominant forms of the O 1s spectra are O^{2-} (530 eV) and OH^- (531.6 eV). At the binding energy of 532.8 eV, crystalline water (lattice water) can be observed on the surface of the $Cr_{2.0}$ specimen. The presence of crystalline water may be attributed to the stability of certain corrosion products (hydroxides) in the hydrated state, forming a protective layer to prevent further corrosion[32]. XPS results show that during the electrochemical corrosion process, the protective film formed by composite corrosion product mainly consists of Fe_2O_3, Cr_2O_3, Al_2O_3, CuO, and their hydroxides, which alleviates the erosion of the alloy in corrosive media and then enhances the corrosion resistance of the alloy.

Fig.12 shows the content comparison of each component on

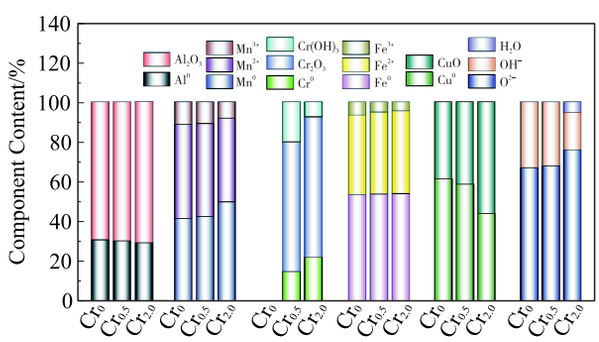

Fig.12 Content comparison of each component on surface of $FeCr_xMnAlCu$ HEAs with x=0, 0.5, and 2.0 in 3.5wt% NaCl solution

surface of $FeCr_xMnAlCu$ HEAs with x=0, 0.5, and 2.0 in 3.5wt% NaCl solution. Al_2O_3, Cr_2O_3, metallic Fe, Mn, and Cu are the main components of the passivation film. Additionally, the oxides formed by element Cr are denser than those formed by Al and Cu[31,33–34]. A slight decrease in the amount of Fe^{3+} in corrosion products and a decrease in the ratio of Mn^{2+} to Mn^{3+} may lead to an increase in density of the passivation films[35]. Therefore, compared with that of Cr_0 specimen, the content of Al_2O_3 and CuO is increased due to the surface passivation film of $Cr_{2.0}$ specimen. Additionally, the presence of Cr_2O_3 significantly enhances the protective effect. As the Cr content increases, O^{2-} gradually increases, OH^- gradually decreases, and bound water appears in the $Cr_{2.0}$ specimen. In conclusion, the addition of element Cr alters the content and composition of the passivation film, impacting the corrosion resistance of HEAs.

3.3 Immersion corrosion performance

The effect of Cr content on the corrosion of $FeCr_xMnAlCu$ HEAs was investigated through immersion experiments. The corrosion rate[20] is calculated according to Eq.(14):

$$\text{Corrosion rate}\,(\text{mm/a}) = \frac{K\Delta W}{TAD} \quad (14)$$

where K is a constant (8.76×10^4), ΔW is the mass consumed by corrosion of the specimen (g), T is the immersion time (h), A is the total surface area of the alloy specimen in solution (cm^2), and D is the specimen density ($g\cdot cm^{-3}$). The average corrosion rate of $FeCr_xMnAlCu$ HEAs after immersion in corrosion solution for 168 h is shown in Fig.13. The corrosion rate of the specimens is gradually decreased with the increase in Cr content, and the $Cr_{2.0}$ specimen exhibits the lowest corrosion rate (0.0292 mm/a), indicating the optimal corrosion resistance. This result is consistent with the electrochemical test results, indicating that the addition of element Cr is beneficial to the corrosion resistance of $FeCr_xMnAlCu$ HEAs in corrosive solution.

3.4 Corrosion mechanism

Fig. 14 depicts the schematic diagrams of the corrosion

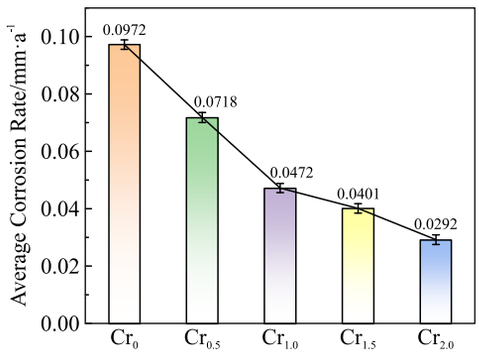

Fig.13 Average corrosion rates of different $FeCr_xMnAlCu$ HEAs after immersion for 168 h

mechanisms of $FeCr_xMnAlCu$ HEAs in 3.5wt% NaCl solution. Fig. $14a_1-14a_3$ show the corrosion processes of the Cr_0 specimen. More active metal elements on the specimen surface form a discontinuous passivation film through chemisorption before the electrochemical corrosion, as shown in Fig. $14a_1$, due to the weak stability of grain boundaries[36] and the presence of Cu-segregation. Some Cl^- with a small radius is adsorbed to the passivation film, and some just passes through the passivation film, maintaining a relatively high current density, and causing the metal cations to become active and disordered. Pitting occurs when the electric field at the film/solution interface reaches a certain critical value, as shown in Fig. $14a_2$. The substrate is exposed to the solution, and the passivation film and locally damaged areas form a large cathode anode, which accelerates the corrosion of $FeCr_xMnAlCu$ HEAs, leading to the formation of larger corrosion holes. At the beginning of corrosion, the difference in reactivity of the metal elements leads to different dissolution rates. The high dissolution rate will affect the low dissolution rate of the elements. Thus, more active metal in the pore acts as the anode. The anodic reaction is expressed by Eq.(15), as follows:

$$M \rightarrow M^{n+} + ne^- \quad (15)$$

At the same time, the electrons released from the metal cations migrate to the surface outside the corrosion hole, which is passivated and acts as a cathode because of its positive potential. Therefore, the inner and outer holes form an activated passivated micro-couple corrosion battery. The cathode reduction reaction occurs at the outside of the corrosion holes, as shown in Eq.(16):

$$O_2 + H_2O + 4e^- \rightarrow 4OH^- \quad (16)$$

The pH value of the electrolyte solution at the corrosion hole increases. The metal cation produces a secondary reaction, and the resultant hydroxide is deposited near the hole, as shown in Eq.(17):

$$M^{n+} + nOH^- \rightarrow M(OH)_n \quad (17)$$

Meanwhile, the micro-couple effect between the grain boundary and grain interior accelerates the electrochemical reaction and forms a passivation film on the face of Cr_0 specimen, as shown in Fig. $14a_3$. With the corrosion proceeding, the pH value outside the corrosion hole continues to increase, leading to a gradual build-up of a large number of hydroxides. This accumulation forms an occlusion cell, hindering the migration of ions inside and outside the holes. After the formation of the occlusion cell, the hydrolysis of more reactive metal cations in the pore and the metal with the more positive potential can be obtained, as expressed by Eq.(18–19):

$$M^{n+} + nH_2O \leftrightarrow M(OH)_n + nH^+ \quad (18)$$

$$2M + nH_2O \leftrightarrow M_2O_n + 2nH^+ + 2ne^- \quad (19)$$

This hydrolysis lowers the pH value in the pore, forming a highly acidic and high Cl^- concentration environment in the pore, and thus promoting the metal corrosion. This corrosion

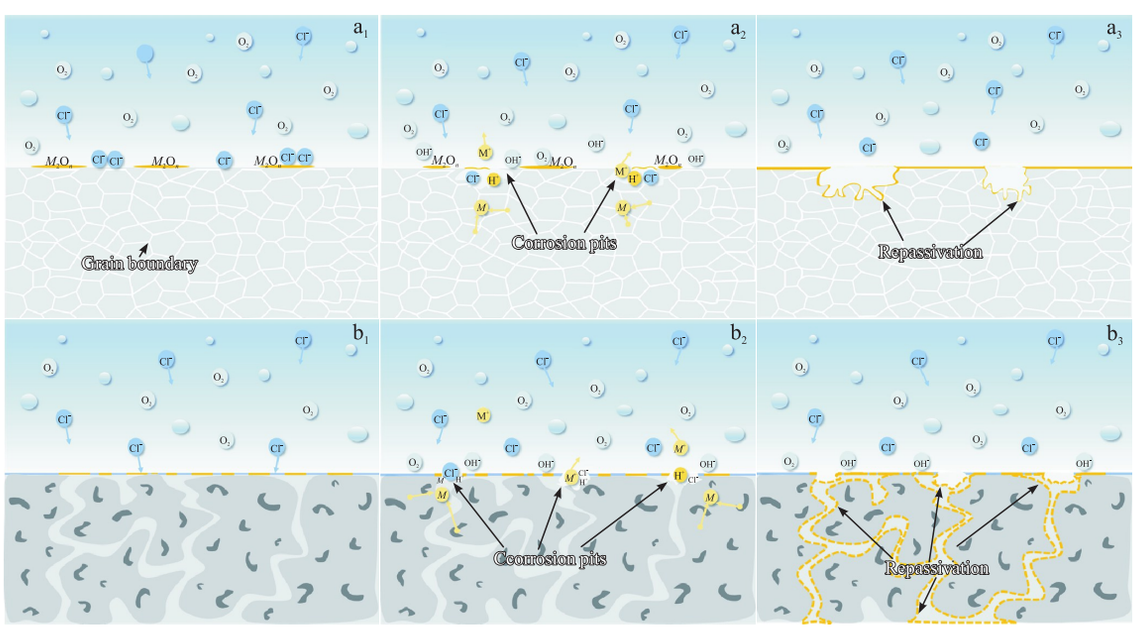

Fig.14 Schematic diagrams of corrosion mechanism of Cr_0 (a_1–a_3) and $Cr_{2.0}$ (b_1–b_3) specimens: (a_1, b_1) before corrosion; (a_2, b_2) during corrosion; (a_3, b_3) after corrosion

causes more Cl^- migration and further acidification of the pore environment. This cycle is repeated during the corrosion process, finally forming an autocatalytic process of intrapore acidification.

Fig. 14b_1 – 14b_3 show the corrosion processes of the $Cr_{2.0}$ specimen. Two kinds of oxide films, Cr_2O_3 and M_2O_3 (such as Al_2O_3), are generated on the specimen surface before the electrochemical corrosion[37], as shown in Fig. 14b_1. In the electrochemical corrosion process, compared with the Cr_2O_3 film, the Al_2O_3 film with lower density and a lower standard electrode potential is more vulnerable to Cl^- in 3.5wt% NaCl solution, preferentially corroding the Al_2O_3 film, forming local galvanic coupling corrosion, and resulting in the occurrence of pitting corrosion, as shown in Fig. 14b_2. With the corrosion proceeding, a corrosion hole is gradually formed on the specimen surface. When a corrosion hole forms, an acidified autocatalytic process occurs within the hole. The electrolyte solution and the alloy matrix undergo a redox reaction with the corrosion proceeding, producing oxides and hydroxides, which are deposited on the specimen surface. A passivation film is then progressively formed at the corrosion site to stop the additional corrosion. The percentage of Cr_2O_3 film in the passivation film is increased with the increase in Cr content in $FeCr_xMnAlCu$ HEAs. Owing to its stability and density, Cr_2O_3 can chemically interact with the surrounding water and other oxides or hydroxides to repair the damaged layer, preventing further corrosion, as shown in Fig. 14b_3. The surface morphologies of $FeCr_xMnAlCu$ HEAs after electrochemical corrosion in Fig. 8 and XPS spectra in Fig. 9 – Fig. 11 also confirm the occurrence of the abovementioned reactions.

4 Conclusions

1) The Cr_0 specimen has bcc single-phase structure with an equiaxial crystalline microstructure. When Cr is added into the alloy, the structure is transformed into a mixed bcc+fcc dual-phase structure with DR and ID formation. Meanwhile, with the increase in Cr content, the Laves phase ($Al_{0.25}Cu_{0.75}$) begins to precipitate.

2) The PDP polarization curve of $FeCr_xMnAlCu$ HEAs shows that Cr in the alloy can spontaneously passivate under natural conditions, forming a passivation film with excellent protective properties. As the Cr content increases, the I_{corr} of the alloy shows a downward trend, while the E_{corr} and charge transfer resistance are both significantly improved. Among them, the $Cr_{2.0}$ alloy exhibits the best corrosion resistance, with I_{corr}=1.991 × 10^{-6} A·cm^{-2}, E_{corr}=−0.354 V vs. Ag/AgCl, and R_p=8622.6 Ω·cm^2. In addition, the immersion corrosion rate of $Cr_{2.0}$ alloy was the lowest (0.0292 mm/a), further confirming its excellent corrosion resistance. These results indicate that the addition of Cr significantly improves the corrosion resistance of $FeCr_xMnAlCu$ HEAs by promoting the formation of passivation films and improving their stability.

3) All $FeCr_xMnAlCu$ HEAs exhibit selective corrosion at the interface of DR and ID structures, and the degree of corrosion is decreased with the increase in Cr content. The corrosion product films of the $FeCr_xMnAlCu$ HEAs mainly contain Al_2O_3, Cr_2O_3, Fe_2O_3, MnO, CuO, and their hydroxides. Due to the smaller density and lower standard electrode potential of the Al_2O_3 film, the formation of local galvanic coupling corrosion between the two films results in the dissolution of the Al_2O_3 film. This dissolution area is covered by regenerated oxide and hydroxide film with a more positive potential, thus effectively inhibiting the infiltration of Cl^-. With the increase in Cr content, the oxide film forming on the surface becomes denser, thus effectively reducing the corrosion rate and degree of $FeCr_xMnAlCu$ HEAs.

References

1 Wei L, Qin W M. *Corrosion Science*[J], 2022, 206: 110525
2 Ma Yi, Du Xiaoyi, Wang Mingliang *et al*. *Materials China*[J], 2025, 44(1): 49 (in Chinese)
3 Ben Q, Zhang Y M, Sun L X *et al. Metals*[J], 2022, 12(9): 1428
4 Pan Chaoyang, Liu Zongde, Shen Yue *et al. Rare Metal Materials and Engineering*[J], 2024, 53(9): 2438 (in Chinese)
5 Xu Qin, Wang Qi, Zhao Jiading *et al. Rare Metal Materials and Engineering*[J], 2024, 53(11): 3194 (in Chinese)
6 Feng L, Wang M Q, Zhao Y C *et al. Rare Metal Materials and Engineering*[J], 2024, 53(1): 85
7 Feng L, Yang Y, Zhao Y C *et al. Corrosion Science*[J], 2024, 233: 112087
8 Feng Li, Wang Zhipeng, Zhao Yanchun *et al. Rare Metal Materials and Engineering*[J], 2024, 53(11): 3175 (in Chinese)
9 Yan X L, Guo H, Yang W *et al. Journal of Alloys and Compounds*[J], 2021, 860: 158436
10 Ge Y Y, Cheng J B, Mo J Y *et al. Journal of Alloys and Compounds*[J], 2024, 976: 173173
11 Chai W K, Lu T, Pan Y. *Intermetallics*[J], 2020, 116: 106654
12 Ren B, Zhao R F, Chen C *et al. Advanced Engineering Materials*[J], 2022, 24(10): 2200224
13 Wang Z P, Ma K, Feng L *et al. Materials Today Communications*[J], 2024, 40: 109864
14 Feng Li, Wang Zhaopin, Zhao Yanchun *et al*. *Rare Metal Materials and Engineering*[J], 2024, 53(12): 3373 (in Chinese)
15 Chen H S, Tsai C W, Tung C C *et al. Annales de Chimie-Science des Materiaux*[J], 2006, 31(6): 685
16 Guo S, Ng C, Lu J *et al. Journal of Applied Physics*[J], 2011, 109: 103505
17 Yang X, Zhang Y. *Materials Chemistry and Physics*[J], 2012, 132(2–3): 233
18 Hsu W, Tsai C, Yeh A *et al. Nature Reviews Chemistry*[J], 2024, 8: 471
19 Zhang Y, Zhou Y J, Lin J P *et al. Advanced Engineering Materials*[J], 2008, 10(6): 534
20 Dhanapal A, Rajendraboopathy S, Balasubramanian V. *Transactions of the Indian Institute of Metals*[J], 2012, 65: 275
21 Lin C, Meng L, Tan M *et al. Intermetallics*[J], 2023, 153: 107781
22 Yakın A, Şimşek T, Avar B *et al. Applied Physics A*[J], 2022, 128(8): 686

23 Xiang C, Fu H M, Zhang Z M *et al*. *Journal of Alloys and Compounds*[J], 2020, 818: 153352

24 Xie F, Zhang X, Zhai C S *et al. Electrochimica Acta*[J], 2024, 507: 145153

25 Lu J Z, Han B, Cui C Y *et al. Optics and Laser Technology*[J], 2017, 88: 250

26 Hong M, Park I, Kim J. *Metals and Materials International*[J], 2017, 23: 708

27 Ben S M, Sabot R, Triki E *et al. Corrosion Science*[J], 2014, 86: 61

28 Wang L, Mercier D, Zanna S *et al*. *Corrosion Science*[J], 2020, 167: 108507

29 Gu X H, Li X R, Zhang Q H *et al*. *Intermetallics*[J],2023, 162: 107994

30 Shi Y Z, Yang B, Xie X *et al. Corrosion Science*[J], 2017, 119: 33

31 Jin Z H, Ge H H, Lin W W *et al. Applied Surface Science*[J], 2014, 322: 47

32 Okamoto G. *Corrosion Science*[J], 1973, 13(6): 471

33 Kharitonov D S, Sommertune J, Örnek C *et al. Corrosion Science*[J], 2019, 148: 237

34 Wang J M, Jiang H, Chang X X *et al. Corrosion Science*[J], 2023, 221: 111313

35 Fajardo S, Llorente I, Jiménez J A *et al. Corrosion Science*[J], 2019, 154: 246

36 Wang Y, Jin J S, Zhang M *et al. Journal of Alloys and Compounds*[J], 2022, 891: 161822

37 Muangtong P, Rodchanarowan A, Chaysuwan D *et al. Corrosion Science*[J], 2020, 172: 108740

$FeCr_xMnAlCu$高熵合金在3.5wt% NaCl溶液中的耐腐蚀性能

冯　力[1,2]，张　娴[1,2]，马　凯[1,2]，赵燕春[1,2]，苓亚军[1,2]，刘瑞龙[1,2]，付　轩[1,2]

(1. 兰州理工大学 材料科学与工程学院，甘肃 兰州 730050)

(2. 兰州理工大学 省部共建有色金属先进加工与再利用国家重点实验室，甘肃 兰州 730050)

摘　要：采用真空电弧熔炼制备$FeCr_xMnAlCu$（x=0，0.5，1.0，1.5，2.0）高熵合金，通过电化学动电位极化曲线和浸泡实验的方法研究了该高熵合金在室温下3.5wt% NaCl溶液中的腐蚀行为。微观组织结果表明，x=0的高熵合金具有体心立方相结构，而x=0.5~2.0时该高熵合金具有面心立方+体心立方双相混合结构。腐蚀结果表明，随着Cr含量的增加，高熵合金的耐腐蚀性能增加。其中，x=2.0时的高熵合金表现出最佳的耐腐蚀性能，具有最高的自腐蚀电位（E_{corr}=−0.354 V vs. Ag/AgCl）、最小的自腐蚀电流密度（I_{corr}=1.991×10^{-6} A·cm^{-2}）和最小的腐蚀速率（0.0292 mm/a）。在腐蚀后的高熵合金表面形成了氧化物和氢氧化物的复合钝化膜，且Cr_2O_3含量随着Cr含量的增加而增加，从而有效地提高了钝化膜的稳定性和保护性能。

关键词：耐腐蚀性能；高熵合金；钝化膜；盐溶液腐蚀

作者简介：冯　力，男，1981年生，博士，教授，兰州理工大学材料科学与工程学院，甘肃 兰州 730050，E-mail：fenglils@lut.edu.cn